Silicon (2024) 16:4843–4856
https://doi.org/10.1007/s12633-024-03056-y

RESEARCH

Synergistic Photocatalysis of Bayerite/Zeolite Loaded TiO_2 Nanocomposites for Highly Efficient Degradation of Organic Pollutants in Aqueous Environments

Abdellah Ait baha[1] · Aziz Ait-Karra[1] · Rachid Idouhli[1] · Kamal Tabit[2] · Othmane Zakir[1] · Burak Dikici[3] · Mohy Eddine Khadiri[1] · Abdesselam Abouelfida[1]

Received: 4 March 2024 / Accepted: 5 June 2024 / Published online: 10 June 2024

Abstract

Methylene blue dye (MB), prevalent in textiles like cotton, wood, and silk, raises environmental and health concerns. This study presents a successful synthesis of a Bayerite/zeolite nanocomposite powder using fumed silica by-product and aluminum nitrate. Hydrothermal exploration of factors, including duration, temperature, and Al/Si ratios, revealed that high temperature (160°C) and short duration (6h) favored optimal crystallization of bayerite/zeolite phases. Subsequently, an integrated photocatalytic adsorbent (IPA) was developed by mechanically mixing the synthesized bayerite/zeolite with TiO_2, followed by calcination (500 °C, 2 h), demonstrating superior efficiency in MB photodegradation under UV–Vis light. The IPA achieved 100% degradation efficiency for 60 mg/L of MB and maintained good photostability over three cycles. The bayerite/zeolite-supported TiO_2 nanocomposite exhibited the generation of positive holes (h +) and active hydroxyl radicals (OH•), showcasing its potential as a promising material for wastewater treatment applications.

Highlights

- Successful synthesis of Bayerite/zeolite nanocomposite powder from fumed silica waste and aluminum nitrate.
- Development of an integrated photocatalytic adsorbent (IPA) by mixing synthesized bayerite/zeolite with TiO2.
- IPA demonstrated superior efficiency in Methylene Blue (MB) photodegradation under UV-Vis light
- The bayerite/zeolite-supported TiO2 nanocomposite maintained good photostability over three cycles, showcasing its potential for wastewater treatment applications.

Keywords Fumed silica · Bayerite · Zeolite · Organic pollutant · Photocatalysis

1 Introduction

Water pollution is a serious problem and significant danger that has a hazardous impact on both aquatic life and the well-being of humans [1]. Even in areas that are now thought to have abundant water, the rise in pollutant percentage that causes global pollution is a severe environmental issue, that can occur as a result of water contamination [2]. Various contaminants, including toxins and industrial or agricultural dyes, contribute to this issue. Exposure to these impurities through tainted water sources can have profound and enduring health consequences, including the development of conditions such as cancer, neurological diseases, and digestive problems [3].

✉ Abdellah Ait baha
abdellah.aitbaha@ced.uca.ma

[1] Laboratory of Applied Chemistry and Biomass, Department of Chemistry, Faculty of Science Semlalia, Cadi Ayyad University, BP 2390, Marrakech, Morocco

[2] LIPIM Laboratory, National School of Applied Sciences, Sultan Moulay Slimane University, P.O. Box 77, Khouribga, Morocco

[3] Department of Mechanical Engineering, Faculty of Engineering, Ataturk University, 25240 Erzurum, Turkey

The increase in industrial activities has led to the emergence of various industrial wastes and organic pollutants, becoming primary sources of environmental contamination. In particular, Methylene Blue (MB), a dye classified in the Thiazine group, is frequently employed in pharmaceuticals, textiles, printing, and other sectors [4, 5]. MB is known for its toxicity and persistence in the environment as it can disrupt aquatic ecosystems and have harmful effects on organisms, leading to reduced biodiversity and environmental imbalances [6]. However, the incorrect disposal of this dye can seriously pollute the water supply. Efforts to mitigate the impact of this pollutant require effective water treatment methods.

Several processes can be employed to remove this industrial dye from water sources namely adsorption [7], ion exchange process [8], electrocoagulation [9], biological treatment process [10], and membrane filtration process [11]. However, these methods are inefficient and lack of desorption process. Furthermore, advanced oxidation processes such as photocatalysis employing materials like TiO_2 or ZnO have demonstrated highly promising outcomes in capturing and removing these pollutants, due to the degradation and complete breakdown of pollutant molecules through oxidation reactions ensuring its reusability [12, 13].

TiO_2 is widely recognized as a highly efficient catalyst for the removal of MB through photocatalysis [14–16]. The robust photocatalytic performance of TiO_2 can be attributed to its capacity for producing reactive oxygen species upon exposure to light, facilitating the efficient degradation of MB molecules [17, 18]. However, two factors in the photodecomposition process can restrict the use of titania oxide semiconductors. Firstly, its wide bandgap utilizes only 3–4% of the solar light spectrum [19, 20]. Secondly, the hole electron pairs generated by UV irradiation are easily recombined, which can reduce its overall efficiency for the photodegradation of MB [21]. Additionally, it was reported that one of the primary issues with using photocatalysis is the energy waste that results from the predominance of this electron–hole recombination since the quantum yield is limited in the absence of an appropriate electron acceptor or donor [22]. Therefore, it is essential to migrate the electron–hole recombination to guarantee the effective photodecomposition of pollutant molecules.

To overcome these limitations and to enhance the activity of TiO_2, significant attention has been devoted to the immobilization of this semiconductor on various supports due to their potential applications in photocatalysis and environmental remediation. This approach aims to augment adsorption capacity and improve separation efficiency without drastically altering the overall structure and stability [23–25]. For instance, recent research by Khanmohammadi et al. (2024) highlighted the use of mesoporous silica matrix as a support material for Cu–Ti–O heterojunction immobilization, demonstrating improved photocatalytic performance for the degradation of tetracycline pollutant [26]. Additionally, the study by Moradi et al. (2014) investigated the immobilization of TiO_2-WO_3 particles on diatomite supports, revealing enhanced photocatalytic activity for paraquat herbicide treatment in agriculture applications [27]. Furthermore, the work by Haghighi et al. (2019) focused on the immobilization of TiO_2/PS composites on titanium dioxide spherical arrays, elucidating the synergistic effects between the semiconductors and the support structure in promoting photocatalytic degradation processes [28]. These studies collectively underscore the importance of exploring diverse support materials and immobilization techniques to harness the full potential of TiO_2 semiconductors in various photocatalytic applications. Accordingly, Materials, such as zeolite, serve as substrates for TiO_2, providing improved surface area and adsorption properties that are quite beneficial.

The exceptional qualities of zeolites, including their porous structure, great hydrothermal stability, catalytic activity, superior shape selectivity, and binding capabilities, make them particularly interesting adsorbents [29–32]. Furthermore, zeolite was extensively utilized as a substrate for TiO_2, thereby enhancing its surface area and enabling better access of MB to TiO_2 [2, 14, 22]. Consequently, this increase contributed to the enhancement of its photocatalytic degradation performance [25, 33]. Similarly, prior researches has shown that boehmite, bayerite, or gibbsite crystalline nanomaterials have strong filtering capabilities because both the surface hydroxyl groups and the aluminum anions participate in the ion exchange process. This involvement may, in turn, restrict TiO2 dispersion [34–36]. Moreover, the use of so-called bayerite/zeolite nanocomposites as the combination of filtration and adsorption processes can be quite beneficial due to their small size and highly reactive character as one of the most broadly used, quick, and affordable technologies for managing groundwater and industrial wastewater [37, 38]. Thus, TiO_2 exhibits remarkable efficiency as a photocatalyst for the removal of MB through photocatalysis.

The removal mechanism of MB using zeolite-TiO_2 composites has been extensively investigated [39, 40]. The mechanism involves the adsorption of MB onto the surface of zeolite, promoting better interaction between MB and the composite. This interaction results in enhanced degradation efficiency, accompanied by the generation of reactive oxygen species (ROS) upon the activation of TiO_2 by light. These ROS then react with the adsorbed MB molecules, breaking them down into smaller, less harmful by-products or CO_2 and H_2O [41]. Despite these favorable attributes, it is important to note certain limitations associated with these composites. One limitation is the possibility of photocorrosion, where the composite's performance may deteriorate over time due to the degradation of TiO_2 in the presence of

light and water [16]. Another limitation is the potential for reusability and stability of the composite, as repeated use and prolonged exposure to environmental conditions can affect its overall performance and efficiency [42].

Recent advancements have shown that the incorporation of bayerite and zeolite as substrates for TiO_2 significantly contributes to the overall performance of the composite [23, 37]. Specifically, zeolite and bayerite exhibit considerable potential as substrates for TiO_2, improving its activity performance and stability, and resulting in enhanced photocatalytic performance. Further exploration and development of these composite systems could lead to the advancement of efficient and sustainable methods for the removal of MB and other organic pollutants from wastewater.

The current research focuses on the synthesis of new pair compounds based on nanocomposites bayerite/zeolite from fumed silica by-product and aluminum nitrate using hydrothermal reaction. The influence of different parameters on the different aspects of bayerite/zeolite crystallization was investigated in detail by structural analysis, morphological properties, and surface area analysis. The removal capacity of bayerite/zeolite-supported TiO_2 photocatalyst was measured by the decomposition of MB dye. However, to the best of our knowledge, no attention was paid to the bayerite/zeolite combined with TiO_2. thus, while using the photodegradation approach, consideration was given to the photocatalyst's properties such as surface area, pH_{pzc} value, hydrophobicity, as well as other experimental measurements.

2 Experimental

2.1 Bayerite/Zeolite synthesis

All chemicals were used straightaway without any additional purification. Aluminum nitrate nonahydrate ($Al(NO)_3$ $9H_2O$, Sigma-Aldrich) and fumed silica were used as alumina and silica sources, respectively. The synthesis of bayerite/zeolite through conventional hydrothermal involved the use of a 60 mL hydrogel with a mass ratio of $1.75Na_2O{:}0.5Al_2O_3{:}3SiO_2{:}150H_2O$. Aluminum nitrate was dissolved in an aqueous solution of sodium hydroxide pellets (99%, Sigma-Aldrich), and fumed silica was subsequently added to the mixture. The resulting hydrogel was placed in a stainless steel autoclave lined with Teflon and hydrothermally treated for 6–48 h at temperatures ranging from 100 to 160 °C after being stirred for 1 h at room temperature.

Throughout the synthesis period, a pH solution of around 8 was achieved by collecting, filtering, and washing the solid products with deionized water. Finally, the filtrates were dried in an oven at 100 °C for 24 h.

2.2 Bayerite/Zeolite characterization

The obtained products were acquired and characterized using several conventional techniques. Powder X-ray diffraction (XRD) patterns were obtained using a RIGAKU D/Max-IIIB diffractometer with Cu radiation, operated at 20 mA and 40 kV. The diffraction patterns were gathered in the 2θ range of 5–85° at a scan speed of 5°/min. SEM images were captured using a Tescan Vega 3 microscope with a cold-field emission gun operating at 2 kV and 10 A. Transmission IR spectra were recorded using a VERTEX70 DTGS spectrometer with a KBr method. The crystallite size of the samples was calculated using the Scherrer equation. Nitrogen adsorption–desorption experiments were carried out under nitrogen degassing at 200°C for 7 h using a micrometrics 3-Flex 5.00 version instrument. The optimum sample was calcined at 300°C for 3 h before photodegradation tests. The density of the optimized sample was measured with a high degree of precision using a pycnometer device. The zeolite-only density was derived by filling the cavities of the particles with Diethyl phthalate. Furthermore, the ion exchange capacity was determined using the cobalthexamine method.

2.3 Preparation of Bayerite/Zeolite-TiO_2 catalyst

The TiO_2 powder, which was purchased from Sigma Aldrich, served as the starting material for the catalyst preparation. Subsequently, an adsorbent-photocatalyst 50:50 wt% sample was prepared from bayerite/zeolite and TiO_2 by mechanical mixing [43]. TiO_2 and the synthesized material were combined and kneaded with the necessary quantity of distilled water. The prepared past was dried at 90 °C for 3 h and subsequently subjected to heating at 500 °C for 2 h to achieve the final Bayerite/zeolite-TiO_2 catalyst.

2.4 Hydrophilicity experiments

The hydrophobicity of the bayerite/zeolite support powder was evaluated to determine its affinity. Wettability experiments were conducted to assess the bayerite/zeolite nanocomposite's interaction with water using the contact angle method, with a focus on its role in the photodegradation of Methylene blue. In a typical experiment, 2 g of zeolite (density = 2.12) was packed into a column with a filling height of 40.48 mm. The column was vertically brought into contact with the surface of a hexane sample to determine the capillary ray. Hexane, selected for its nonpolar nature, possesses a density of 0.65, viscosity of 0.309 mPa·s, and surface tension of 18.4 $mN{\cdot}m^{-1}$ at room temperature and atmospheric pressure. Subsequently, the contact angle was measured using the capillary ray method with 2 g of zeolite and distilled water. Distilled

water, characterized by a surface tension of 72.8 $mN{\cdot}m^{-1}$, was used over a specified integration time of 30 s. These experiments aimed to provide insights into the hydrophilic properties of the bayerite/zeolite nanocomposite and its potential influence on the photocatalytic degradation of Methylene Blue.

2.5 Photocatalysis procedure

Methylene blue (Aldrich 99%) was subjected to photocatalytic degradation in aqueous solutions. The photocatalytic process utilized a 300 W Xe-lamp (white LEDs) with a high-pressure tungsten filament as the UV–visible light source (Brand, Ltd. China). The lamp was positioned at a distance of 20 cm from the solution. Reactions were conducted both in the absence and presence of a photocatalyst. Various initial concentrations of Methylene blue (MB) were introduced into 100 mL of the solution. The experimental setup is schematized in Fig. 1.

To establish adsorption–desorption equilibrium, each suspension was agitated for 60 min in a dark box before initiating illumination with the visible light source. The irradiation phase commenced afterward and extended for 4 h, maintaining the reaction system's temperature at 25 °C. At regular one-hour intervals during the photoreaction, samples were withdrawn using a 15 mL syringe, centrifuged, and separated. The changes in MB solution concentrations were assessed at 666 nm using a 2 mL cylindrical glass reactor fitted with an inner quartz tube. This reactor was equipped with a UV–vis spectrophotometer, specifically a Spectroscan50, featuring a pen-ray mercury lamp ($\lambda = 365$ nm, $I_0 = 4400\ W{\cdot}cm^{-2}$).

The degradation efficiency (DE%) and adsorbed amounts (Qa) of MB were calculated by the change in absorbances by the following equations:

$$DE(\%) = \frac{(C_0 - C_t)}{C_0} \times 100 \tag{1}$$

$$Q_a = \frac{(C_0 - C_t)}{m_c} \times V \tag{2}$$

where $DE(\%)$, Q_a (mg/g), C_0 ($mg{\bullet}L^{-1}$), C_t ($mg{\bullet}L^{-1}$), V (L), and m_c (g) are the degradation efficiency, adsorbed amount, initial MB concentration, MB concentration at different times, solution volume, and mass photocatalyst, respectively.

It is significant to note that the Langmuir–Hinshelwood model predicts that the photodegradation of MB follows pseudo-first-order kinetics. Consequently, the following equation might be used to represent the rate of MB photodegradation:

$$lnC_t = lnC_0 - kt \tag{3}$$

The slopes of the straight-line part of the plots of lnC_t vs t as a function of the experimental parameters were utilized to compute the rate constants (k_t).

Utilizing a commercial TiO_2 photocatalyst that responds to UV light, identical tests were conducted to compare the photocatalytic activities.

2.6 Determination of active radicals

The investigation of the photocatalytic mechanism for Methylene blue (MB) decomposition by the bayerite/zeolite-TiO_2 nanocomposite under irradiation conditions

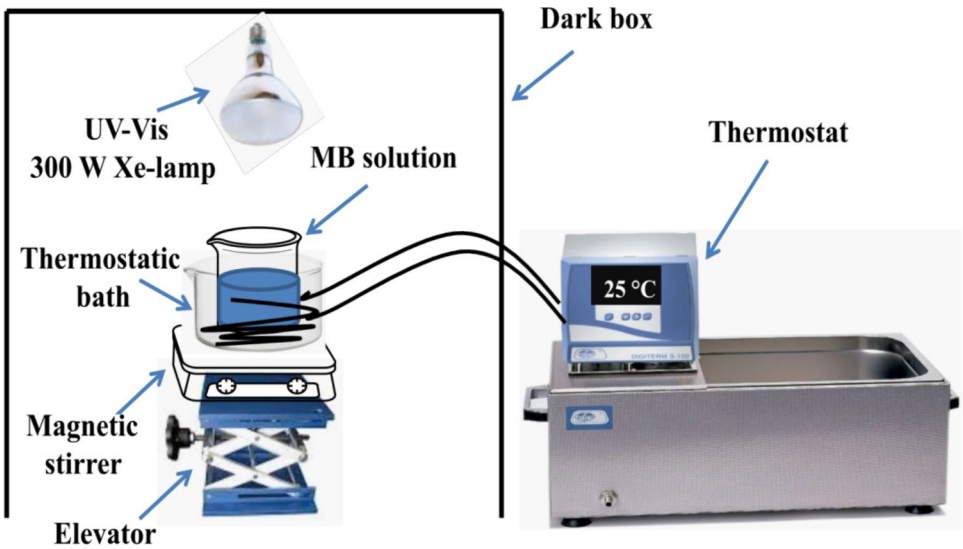

Fig. 1 Experimental setup of MB degradation

was conducted in detail. The aim is to elucidate the photocatalytic reaction pathway and identify the types of photogenerated reactive species responsible for MB degradation on the surface.

In order to understand the involvement of various active species in the degradation process, different scavengers were separately employed to eliminate the relevant active species. The formation of radicals was detected using three chemical scavengers used to capture hydroxyl radicals (OH•), positive holes (h +), and electron and superoxide anion radicals (e −, O_2•$^-$), specifically tert-butyl alcohol, triethanolamine Diamine Tetra-acetic Acid EDTA-2Na, and L-Ascorbic Acid (ASC), respectively.

Furthermore, the roles of these primary active radicals were investigated where a mixture of MB and added traps (4 mM) was stirred with the nanocomposite catalyst and irradiated under the same conditions. Consistent with previous research findings, the OH• radicals generated a variety of intermediate products before achieving complete mineralization, resulting in the generation of CO_2 and H_2O [44, 45].

3 Results and discussion

3.1 Bayerite/zeolite synthesis

3.1.1 Effect of crystallization time

The microstructure evolution of bayerite/zeolite phases from $1.75Na_2O{:}0.5Al_2O_3{:}3SiO_2{:}150H_2O$ mixture at 90°C was systematically investigated by mean of XRD and FTIR measurements, focusing on the impact of synthesis time (ranging from 6 to 48 h). As seen from the trend of XRD patterns in Fig. 2**,** the synthesis duration of 6h promoted the formation of o Bayerite phase (B) with the appearance of weak peaks corresponding to the quartz phase (Q). This observation suggests the persistence of some initial material of fumed silica. With the increase in synthesis time, a decrease in XRD peak intensities was noted, indicating near completion of the bayerite crystallization within the initial 6 h due to its hexagonal structure and simple units. Consequently, a significant portion of the aluminum nitrate was transformed into bayerite during the shorter crystallization period.

Figure 3 presents the FT-IR spectra of samples at various reaction periods. Samples crystallized at 90 °C for 6 h exhibit characteristic bands of bayerite and aluminosilicate, some of which diminish with increased synthesis time. The bands in the range of 1300–450 cm^{-1} are associated with aluminosilicate species such as Si–O-Al, Si–O-Si, and Al-O [46, 47]. In detail [48, 49], the IR band at 470 cm-1 is attributed to vibrations of internal bonds (T-O) of SiO4 and AlO4 tetrahedra. The vibrations at about 551 cm^{-1} are attributed to external

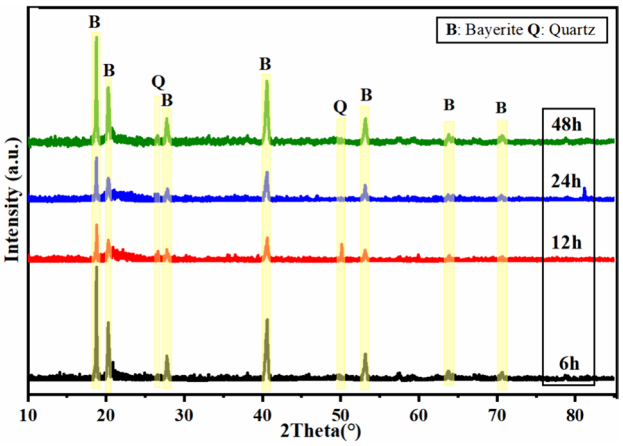

Fig. 2 X-ray diffraction patterns of materials at various stages of synthesis

bonds of double five-membered rings. The bands observed at about 802 cm^{-1} are related to symmetric stretching of external bonds between tetrahedra. The strongest absorption peak at about 1104 cm^{-1} corresponds to the internal asymmetric stretching of Si–O-T bonds. Transmittance bands around 1386 cm^{-1} and 1555 cm^{-1} can be attributed to N–O species. The gradual decrease in transmittance bands around 1445 cm^{-1} and 1365 cm^{-1} over time indicates a reduction in the amorphous material content in the sample [50]. This reduction is due to the gradual transformation of the amorphous phase into crystalline bayerite and aluminosilicate phases. The band at 1647 cm^{-1} observed in the samples is related to the vibration of water molecules within the zeolite [51, 52]. The transmittance band at 3374 cm^{-1} is linked to the airborne water physically absorbed. Surface hydroxyl groups of Al–OH are responsible for the FTIR band at 1104 cm^{-1}. The spectra also confirm that the synthetic aluminum hydroxide nanofiller Al–OH corresponds to bayerite [34], as indicated by the distinctive stretching bands at 3661–3858 cm^{-1}. These various characteristic bands provide insights into the molecular composition and structural changes during the synthesis process. The FTIR and XRD data exhibit excellent agreement, providing a comprehensive understanding of the structural evolution during bayerite/zeolite synthesis.

3.1.2 Effect of crystallization temperature

The influence of crystallization temperature on the synthesis of bayerite/zeolite nanocomposites was investigated, with a focus on the XRD patterns of samples produced at various temperatures within the range of 100 °C to 160 °C after 6 h of crystallization (Fig. 4).

These patterns revealed the formation of a unique zeolite known as Aluminum silicate hydrate (ASH). As the incubation temperature increased from 100 °C to 160 °C, both ASH

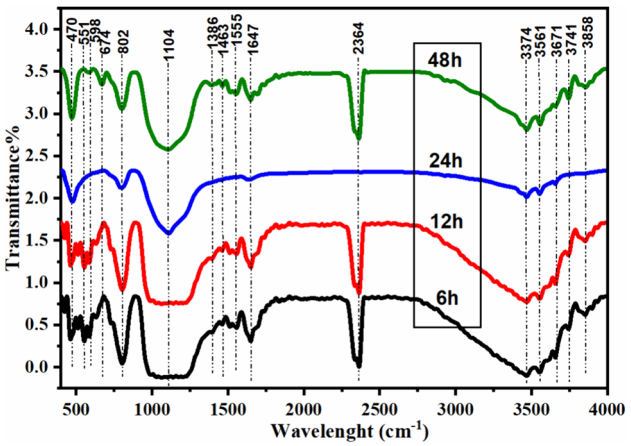

Fig. 3 IR spectra of obtained samples at different synthesis times

and Bayerite's crystallinity exhibited steady growth. This phenomenon can be attributed to the influence of the reaction temperature on the crystallization and nucleation processes, where higher temperatures facilitate more energy and shorter crystallization times. Additionally, higher temperatures can lead to an increased concentration of a chemical group in the solution, which is advantageous for the formation of crystalline materials. This observation of ASH aligns with Ostwald's law of consecutive transformation, suggesting that this zeolite was formed through the transformation of aluminum nitrate and fumed silica into a thermodynamically stable zeolite segment [53] [54]. Nevertheless, crystallization at 160 °C resulted in the formation of pure phases consisting of Bayerite/zeolite composite with traces of quartz.

Figure 5 displays SEM images of samples along with their EDS analysis outcomes, providing insights into structures with an approximate diameter of 10 µm. Octahedral-shaped samples were obtained within the temperature range of 100

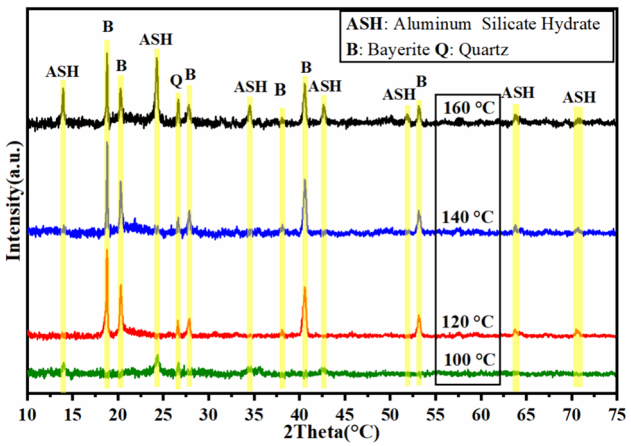

Fig. 4 X-ray diffractograms of data obtained at various synthesis temperatures

°C to 160 °C. The SEM images reveal the presence of numerous zeolite and hydroxide crystals, with some exhibiting a hexagonal shape. It is worth noting that samples synthesized at higher temperatures displayed larger mean crystal diameters and thicknesses. Upon raising the temperature to 160 °C, the octahedral morphology disappeared, giving way to lepispherical particles of aluminum silicate. The SEM images also reveal the presence of a few damaged microspheres within the gel particles. These observations align with the XRD and IR data and indicate the formation of hollow solid structures.

3.1.3 Effect of Al_2O_3/SiO_2 mass ratio

The influence of the Al_2O_3/SiO_2 ratio on the structure of the final products (hydrothermally treated at 160°C for 6 h) was explored. Bayerite and zeolite were synthesized at mass ratios of 2.0, 2.5, and 3.8 by varying the quantity of aluminum nitrate.

The XRD diffractograms are presented in Fig. 6. As observed when the molar composition is 3.8, the powders derived from the synthesis hydrogel exhibit an amorphous phase, indicating a less defined crystalline structure. The sample produced at an Al_2O_3/SiO_2 ratio of 2.5 is attributed to bayerite and poorly crystallized Aluminum Silicate. However, at an Al_2O_3/SiO_2 mass ratio of 2.0, high-purity and well-crystallized bayerite/zeolite were formed, as evident in the XRD diffractogram.

Figure 7 presents SEM micrographs of samples, accompanied by their EDS analysis outcomes, illustrating variations in Al_2O_3/SiO_2 ratios. It is clear that the aggregates in the samples ($Al_2O_3/SiO_2 = 2.0$, 2.5, and 3.8) consist of densely packed crystals. However, unique morphologies resulting from the presence of hydroxide and zeolite can be observed in the $Al_2O_3/SiO_2 = 2.0$ sample. Additionally, the sample produced at $Al_2O_3/SiO_2 = 2.5$ exhibits a similar micrograph. This observation implies that the formation of a double four-membered ring (D4R) is more likely when there is a higher concentration of Al^{4+} in the solution [55]. This suggests that bayerite/zeolite is most likely produced at a lower Al_2O_3/SiO_2 ratio.

In summary, the optimal conditions for the synthesis of high-purity bayerite/zeolite involve a hydrothermal temperature of 160 °C, a shorter synthesis duration of 6 h, and a lower Al/Si mass ratio of 2.0. The crystallite sizes of bayerite and zeolite are 76.8 nm and 60 nm, respectively. The development of nanoporosity in this composite was confirmed by employing the BET technique to measure the specific surface area, as shown in Fig. 8. The specific area was determined to be 24.81 m^2/g. The pore size distribution curve obtained using the Barrett-Joyner-Halenda (BJH) method revealed an average volume pore of 0.163827 cm^3/g, with adsorption and desorption pore sizes centered at 4.07 nm and 4.92 nm, respectively.

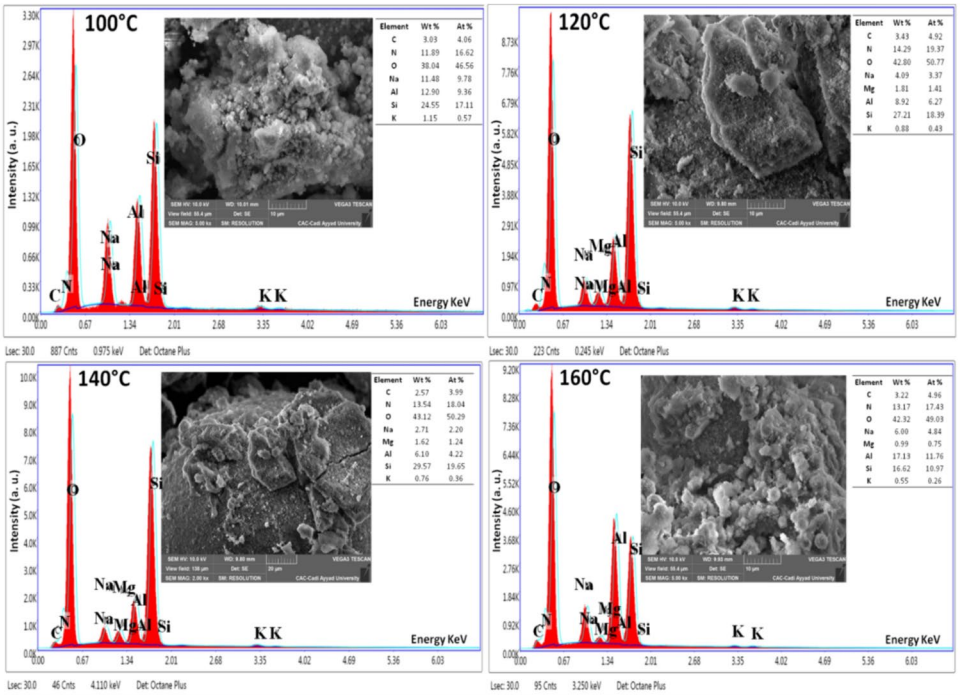

Fig. 5 SEM images of samples obtained at different synthesis temperatures

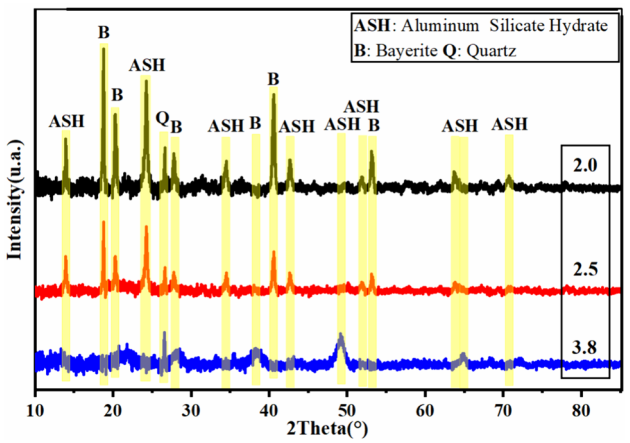

Fig. 6 X-ray diffraction patterns of samples synthesized in the synthesis gel with different Al_2O_3/SiO_2 mass ratios

Furthermore, the ion-exchange capacity (IEC), capillary ray, and contact angle of the optimized composite were measured to be 35 meq/100g, 0.07 µm, and 75.24 degrees, respectively, falling within the typical range for zeolite's IEC and wettability. These findings align with existing literature on similar nanocomposite systems [30, 37, 56].

3.2 Photodegradation testing

The investigation into the photodegradation of Methylene Blue (MB) at an initial concentration of 60 mg/L and pH 12 was conducted, with comparisons made between TiO_2 and Bayerite/zeolite-TiO_2 photocatalysts. The results have been summarized in Fig. 9a and b, revealing notable insights into the photolytic and photodecomposition behavior under UV–vis light irradiation.

In both figures, it is evident that the photolysis of MB did not affect its photodecomposition. Analogous behavior was observed by different researchers [33, 43, 57]. The presence of TiO_2 helped reach a removal rate of 82.2%, showcasing its efficacy in the photodegradation process. Moreover, MB is adsorbed quite strongly on the bayerite/zeolite-TiO_2 surface, reaching 100%, indicating a robust adsorption capability of MB on the composite surface. The adsorption step is an important factor since bayerite/zeolite sorption capability enhanced the photocatalytic activity of TiO_2.

The kinetics follow-up data of the same initial concentration are presented in Fig. 10. The linear projections $lnC_t = lnC_0 - kt$ exposed that they practically matched the pseudo-first-order model. The higher R^2 reveals that the second-order kinetic law provides a more accurate description of the kinetic, which is reflected by the responsive fixation of solutes on the most reactive sites and photocatalyzed. The rate constant (k) and regression coefficients are presented, further supporting the conclusion that the photocatalytic degradation follows pseudo-first-order kinetics.

However, key parameters influencing the efficiency of the photocatalyst were identified. The results indicated that a pH solution of 12, a mass photocatalyst of 1.5 g/L, and an initial concentration of 60 mg/L are the optimum level factors. Under these conditions, the photocatalyst demonstrated

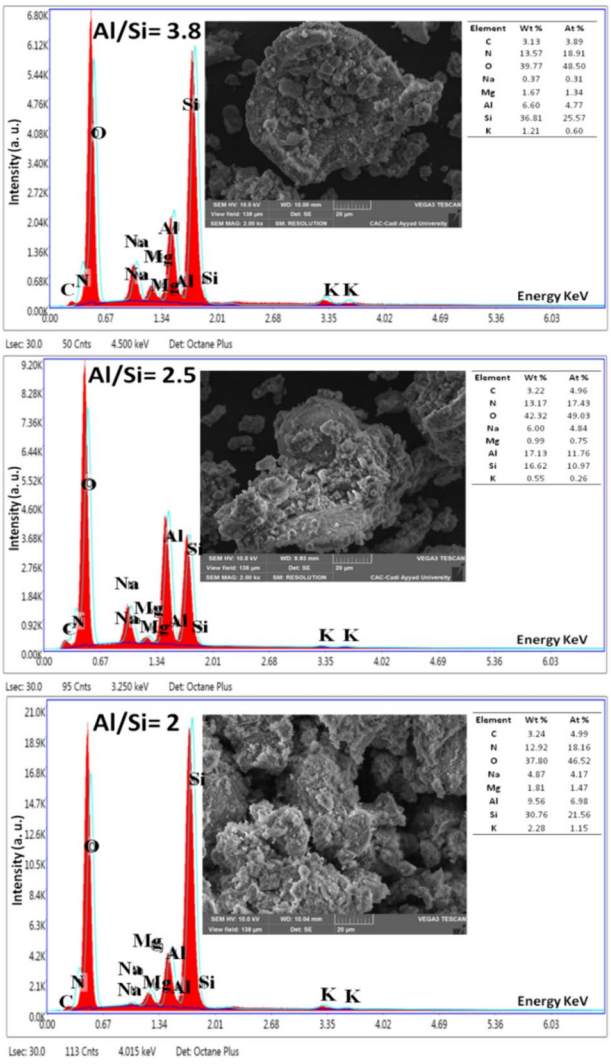

Fig. 7 SEM images of synthesized samples with different Al_2O_3/SiO_2 mass ratio

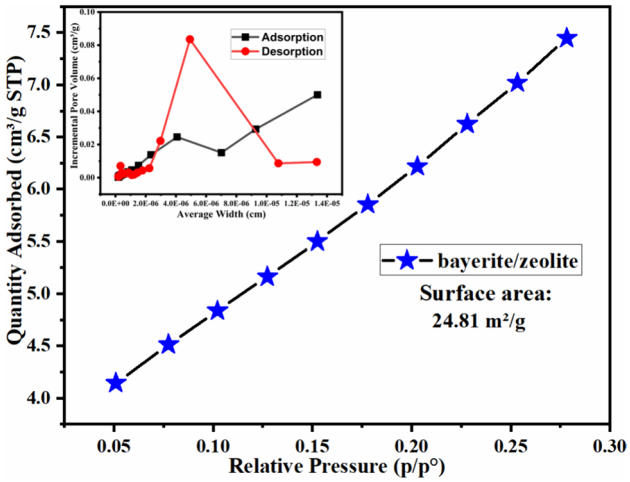

Fig. 8 Specific area and pore size distribution of the Bayerite/zeolite nanocomposite

efficient degradation, achieving complete removal (100%) of MB within 1 h of adsorption and 4 h of irradiation. These findings underscore the importance of optimizing environmental conditions for maximum photocatalytic efficiency [13].

- Choice of initial pH of the solution

One of the most important variables influencing the efficiency of the photocatalytic process is the pH solution, with a profound impact on the surface properties and charge states of the bayerite/zeolite-TiO_2 photocatalyst. Previous research indicates that due to the numerous functions of the photocatalyst, understanding the impact of pH on its productivity is quite challenging [22, 33].

The first is connected to the oxidation states of the bayerite/zeolite-TiO_2 surface, which, following the subsequent processes, is positively charged under an acidic environment and negatively charged under a basic one. This phenomenon is associated with reactions involving hydroxide ions and protons:

$$Al(OH)_3 + H^+ = Al(OH)_4^+$$

$$Al(OH)_3 + OH- = AlO_2 - + 2H_2O$$

$$Na_{2.16}(Al_2Si_{1.68}O_{8.24}H_{2.6})OH + H^+ = Na_{2.16}(Al_2Si_{1.68}O_{8.24}H_{2.6})OH_2{}^+$$

$$Na_{2.16}(Al_2Si_{1.68}O_{8.24}H_{2.6})OH + OH^- = Na_{2.16}(Al_2Si_{1.68}O_{8.24}H_{2.6})O^- + H_2O.$$

$$TiOH + H^+ = TiOH_2^+$$

$$TiOH + OH^- = TiO^- + H_2O$$

The second is the interaction between positive holes and hydroxide ions, which results in the production of hydroxyl radicals. At high or neutral pH values, hydroxyl radicals are thought to predominate, but at low pH levels, positive holes are thought to be the main oxidation species [58].

To assess the primary effect of the solution's pH on the photocatalytic degradation of MB on the surface of the bayerite/zeolite-TiO_2 photocatalyst, the pH drift method was employed. Solutions with varying pH values (pH 2, 3.3, 11.3, and 12) were prepared with NaCl (0.01 M), and 1.5 g/L of zeolite was added. The mixtures were stirred for 72 h, and the pH of the solutions was subsequently measured. The pHpzc (point of zero charge) of the photocatalyst is determined by the intersection of the curves (initial pH) = f (initial pH) and (final pH) = f (final pH), as illustrated in Fig. 9c. The pHpzc was found to be 10.8.

As a result, for a solution with a pH greater than the pHpzc, the adsorption of MB on bayerite/zeolite-TiO_2 is favored. For solutions with a pH lower than the pHpzc, the surface of the photocatalyst becomes positively charged, leading to a potential repulsion of the dye cations. Therefore, as the pH increases, the proportion of negatively charged

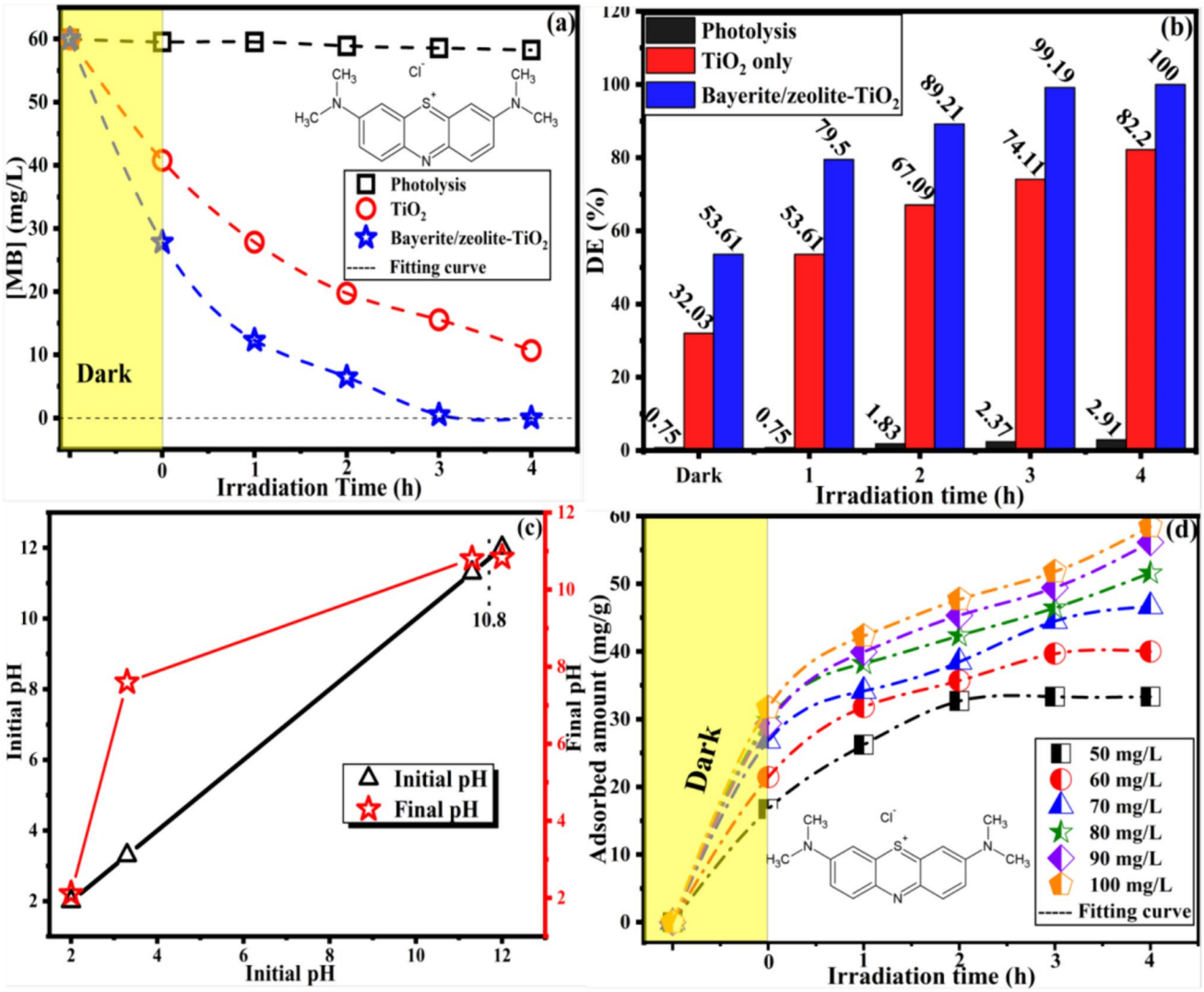

Fig. 9 Experimental degradation data of MB on Bayerite/zeolite-TiO_2 surface by photocatalysis (tungsten filament—lamp 300 W)

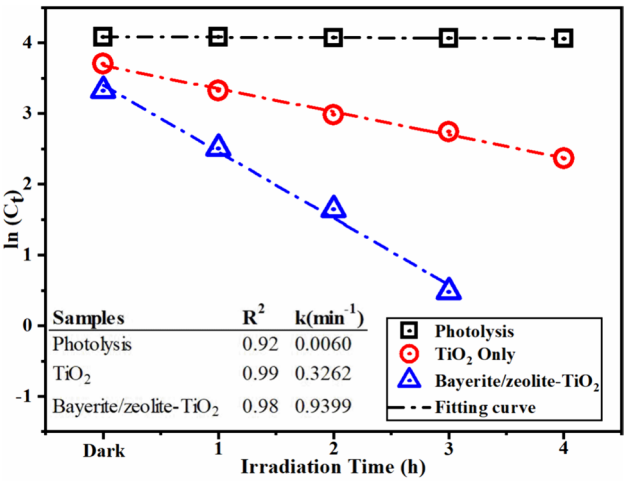

Fig. 10 Kinetics follow-up of degradation data of MB on Bayerite/zeolite-TiO_2

sites on the photocatalyst's surface increases while the proportion of positively charged sites decreases [51]. This understanding is crucial in optimizing the environmental conditions for enhanced photocatalytic performance.

- Effect of initial concentration of the solution

The initial concentrations of the solutions used in this investigation ranged from 40 to 100 mg/L. Fresh solutions were prepared as needed for the experiments. In each case, 100 ml of the solution was added to the reactor, stirring commenced, and the light source was turned on. As shown in Fig. 9d, it is evident that the adsorbed amount at equilibrium increases with the concentration of solution. This phenomenon is indicative of the significant influence of concentration on the photocatalysis rate. Higher dye concentrations accelerate the diffusion of dye molecules from

the solution to the adsorbent's surface, a behavior attributed to the abundance of active sites available on the surface of bayerite/zeolite at the beginning of the adsorption process and during photocatalysis with TiO_2.

However, over time, the photocatalysis rate decreases for higher concentrations due to a saturation phenomenon. This can be explained by the occupation of previously vacant sites on the adsorbent's surface and the emergence of repulsive forces between the adsorbed dye molecules on the photocatalyst and those in the solution. The insulating nature of zeolite further contributes to this effect. Some authors have attributed this occupancy to the formation of intermediates during the photodecomposition [2, 45]. In summary, at an initial concentration of 100 mg/L, 58.47 mg/g of MB molecules were adsorbed with a degradation efficiency of 87.7% within 5 h of the reaction. This finding emphasizes the intricate interplay between initial concentration, adsorption dynamics, and photocatalytic efficiency, providing valuable insights for optimizing the photocatalytic process under varying dye concentrations. In comparison, the photocatalytic performance of Bayerite/zeolite-TiO_2 composites towards methylene blue was significantly better than that of the zeolite-TiO_2 photocatalysts reported in the literature in terms of photocatalytic dose, MB concentration and degradation efficiency (Table 1).

Type of photogenerated reactive species responsible for MB deterioration and their mechanism

Understanding the primary reactive species responsible for the photodegradation process of MB on the bayerite/zeolite-TiO_2 surface is crucial in unraveling the intricate photocatalytic mechanism. Trapping experiments employing chemical scavengers shed light on the nature of these species and their contributions to the degradation process.

Figure 11 depicts the results of trapping experiments using tert-butyl alcohol and Ethylene Diamine Tetra-acetic Acid (EDTA). As can be seen, the addition of tert-butyl alcohol or Ethylene Diamine Tetra-acetic Acid (4 mM) inhibits the kinetic follow-up and the degradation efficiency of MB from 100 to 94%. These results suggest that photogenerated hydroxyl radicals (OH•) and positive holes (h^+) in the valence band are the primary reactive substances in the photocatalytic reaction pathway.

Moreover, superoxide radicals ($O_2\bullet^-$) were not involved in the photodegradation since L-Ascorbic acid was experimented to be a direct electron acceptor and has been used to promote the photodecomposition rate [19]. In addition, it was found that the L-ascorbic acid powder intervened in the improvement of the equilibrium adsorption stage [59]. All in all, according to the reactions, positive holes are trapped by the H_2O molecules to generate hydroxyl radicals which can oxidize MB molecules, and L-Ascorbic acid having reductant properties prevents the electron–hole recombination forming more hydroxyl radicals [24, 59]. Thus, the addition of optimal concentration of L-Ascorbic acid $C_6H_8O_6$ would have a valuable effect on the photocatalytic degradation of MB (100%).

$$Al(OH)_3 + H^+ = Al(OH)_4^+$$

$$L - \text{ascorbic acid} + e^- = OH\bullet + CO_2$$

$$L - \text{Ascorbic acid} + O_2\bullet - = OH\bullet + OH - + CO_2$$

$$L - \text{Ascorbic acid} + OH\bullet = HO_2\bullet + H_2O$$

$$HO_2\bullet + OH\bullet = H_2O + O_2.$$

In summary, when the photocatalyst absorbs energy above the energy of its energy band, electrons are stimulated from the valence band to the conduction band, as shown in Fig. 12. Nevertheless, the former still has holes in it. Since L-Ascorbic acid is an electron scavenger, the created holes directly interacted with MB molecules, H_2O, or OH^- adsorbed in the photocatalyst surface to generate the active species as shown by the equations below. Finally, using a bayerite/zeolite-TiO_2 nanocomposite, the hazardous MB dye decomposes into fairly benign H_2O, CO_2, and simple molecules when exposed to photogenerated holes (h^+) and hydroxyl-radicals (OH•). These findings are consistent with earlier studies and contributes valuable insights into the photocatalytic degradation mechanism of hazardous dyes [18, 33, 36, 45].

$$\text{Bayerite/zeolite} - TiO_2 + h\upsilon \rightarrow e^-CB + h^+VB \rightarrow \text{heat} \quad (4)$$

Table 1 Comparison of photocatalytic performance with other previously reported photocatalysts for the degradation of the pollutant MB

Photocatalysts	Catalyst dose	MB concentration	Degradation efficiency	Ref
TiO_2-zeolite	0.1 g/100 mL	20 ppm	97.32% in 3 h	[60]
CdS/TiO_2/CeO_2-zeolite	0.15 g/100 mL	10 mg/L	99.9% in 2 h	[61]
TiO_2-zeolite	0.2 g/100 mL	20 mg/L	98.25% in 50 min	[62]
RGO/TiO_2/Zeolite-4A	0.3 g/100 mL	25 ppm	100% in 80 min	[63]
TiO_2-Coated NaY	0.1/250 mL	50 ppm	100% in 4 h	[64]
Fe^{3+}/TiO_2-zeolite	0.1 g/100 mL	25 mg/L	92%% in 90 min	[65]
TiO_2-ZSM-5	0.055 g/100 mL	10 mg/L	99.08% in 2 h	[14]
TiO_2/NaY	0.2 mg/100 mL	10 mg/L	88%	[66]
Bayerite/zeolite-TiO_2	0.15 g/100 mL	60 mg/L	100% in 4 h	This study

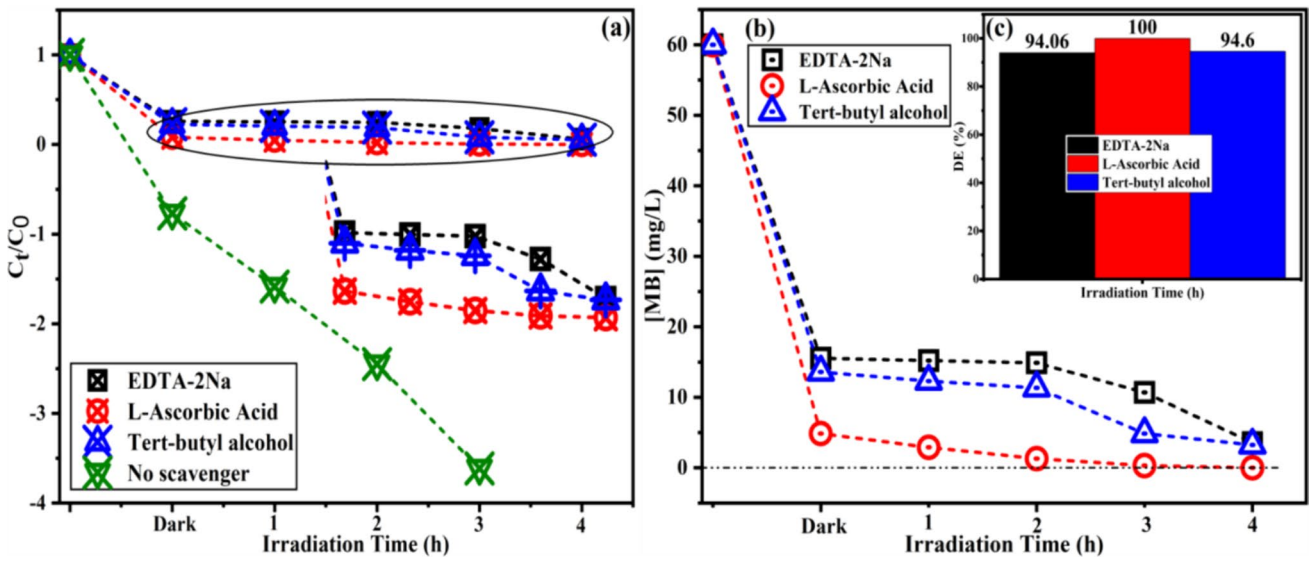

Fig. 11 Effect of radical scavenger addition on the photodecomposition of MB

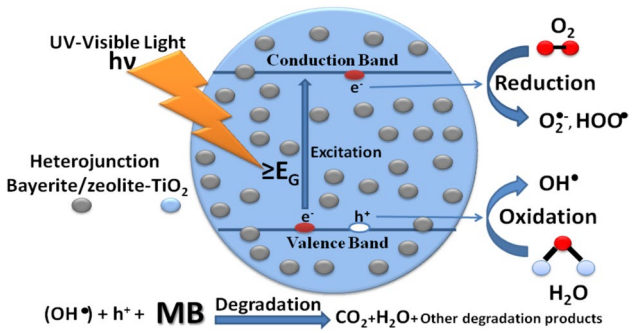

Fig. 12 schematic diagram of the photocatalytic mechanism of bayerite/zeolite-TiO_2

$$h + VB + H2Oads \rightarrow H + + OH\cdot \quad (5)$$

$$h^{+}VB + OH^{-}ads \rightarrow OH \bullet ads \quad (6)$$

$$MB + h^{+}VB \rightarrow \text{Oxidation products} \quad (7)$$

$$MB + OH \bullet + h^{+} \rightarrow CO_2 + H_2O + \text{simple molecules} \quad (8)$$

- Recyclage and reusability efficiency

Assessing the recyclability and reusability of Bayerite/zeolite-TiO2 is vital for its practical application in wastewater treatment. The study focused on the stability and performance of the photocatalyst over multiple usage cycles.

During each photocatalytic cycle, the powder was filtered, washed with ethanol and distilled water, and then dried for 12 h at 80°C. This process was repeated three times using the same photocatalyst. This regeneration process aimed to ensure the removal of any residual contaminants and restore the photocatalyst's active surface.

For the MB concentration solution of 60 mg/L, the photocatalyst exhibited good stability during the second use, achieving a degradation efficiency of 100%. This indicates that even after the first cycle, the photocatalyst retained its efficacy. However, a gradual decrease in efficiency was observed during the third use, reaching 93%.

These findings underscore the promising recyclability and reusability of Bayerite/zeolite-TiO_2, making it a reliable candidate for multiple water treatment cycles. The observed decrease in photocatalytic activity in the third use may be attributed to the poisoning of the photocatalyst's active surface or the occupation of active sites by intermediates that have strongly adsorbed to the surface of the photocatalyst [41].

It can be concluded above results and discussion that the synthesized bayerite/zeolite nanocomposite, especially when coupled with TiO_2, presents itself as a promising candidate for advanced photocatalytic applications in wastewater treatment. The multifaceted analysis conducted in this study lays the groundwork for future research endeavors aimed at refining and optimizing the performance of such nanocomposite materials for sustainable water treatment solutions.

4 Conclusion

In this study, we successfully fabricated a bayerite/zeolite nanocomposite utilizing fumed silica and aluminum nitrate as the silica and aluminum sources, respectively. The physicochemical properties, morphology, crystal size, and nucleation of the final products were significantly influenced by factors such as the selection of silicon and aluminum sources, crystallization duration, temperature, and Al_2O_3/SiO_2 mass ratio. Our findings reveal that a well-developed bayerite/zeolite composite can be achieved after 6 h of hydrothermal treatment at 160 °C, with an Al_2O_3/SiO_2 mass ratio of 2.0 leading to the formation of pure and well-crystallized bayerite/zeolite.

The bayerite/zeolite-TiO_2 nanocomposite demonstrated exceptional photocatalytic activity in degrading methylene blue (MB), achieving complete (100%) degradation of 60mg/L within 1 h of adsorption and 4 h of illumination. This degradation can be attributed to the generation of positive holes and hydroxide radicals. The significant insights gained from this study contribute to the advancement of efficient wastewater treatment technologies, offering promising avenues for preserving our precious water resources. These results hold particular relevance for researchers and practitioners in the field of powder technology, paving the way for the development of innovative materials for environmental applications.

Acknowledgements The authors gratefully acknowledge the help provided by the Center of Analysis, Characterization (CAC), Innovation Center (IC) at Caddy Ayyad University (Marrakech, Morocco), and the Department of Mechanical Engineering, Faculty of Engineering, Ataturk University, 25240 Erzurum, Turkey

Author contributions A. Ait Baha handled all the experiments and wrote the main manuscript text. R. Idouhli and K. Tabit corrected the manuscript. A. Ait-karra and O. Zakir helped with the experiment part. B. Dikici helped with the material analysis. M. Khadiri, and A. Abouelfida supervised the present work. All authors reviewed the manuscript.

Funding The author(s) received no financial support for the research, authorship, and/or publication of this article.

Declarations

Ethics approval Not Applicable (as the results of studies do not involve any human or animal).

Consent to participate Not applicable.

Consent to publish Not applicable.

Competing interests The authors declare no competing interests.

References

1. Kuang S, Xi Q (1997) Electrochemistry for a cleaner environment. Chem Soc Rev 26:181–189. https://doi.org/10.1039/CS9972600181
2. Gou J, Ma Q, Deng X et al (2017) Fabrication of Ag2O/TiO2-Zeolite composite and its enhanced solar light photocatalytic performance and mechanism for degradation of norfloxacin. Chem Eng J 308:818–826. https://doi.org/10.1016/J.CEJ.2016.09.089
3. Beitollahi H, Tajik S, Garkani Nejad F, Safaei M (2020) Recent advances in ZnO nanostructure-based electrochemical sensors and biosensors. J Mater Chem B 8:5826–5844. https://doi.org/10.1039/d0tb00569j
4. Ghanadzadeh Gilani A, Ghorbanpour T, Salmanpour M (2013) Additive effect on the dimer formation of thiazine dyes. J Mol Liq 177:273–282. https://doi.org/10.1016/J.MOLLIQ.2012.09.005
5. Ait-karra A, Zakir O, Mourak A et al (2024) Elaboration of CuS nanomaterials via hydrothermal route: Examining physical properties and photocatalytic potential. J Phys Chem Solids 185:111771. https://doi.org/10.1016/J.JPCS.2023.111771
6. Zhang J, Wang B, Cui H et al (2014) Synthesis of CeO2/fly ash cenospheres composites as novel photocatalysts by modified pyrolysis process. J Rare Earths 32:1120–1125. https://doi.org/10.1016/S1002-0721(14)60192-7
7. Holt PK, Barton GW, Mitchell CA (2005) The future for electrocoagulation as a localised water treatment technology. Chemosphere 59:355–367. https://doi.org/10.1016/j.chemosphere.2004.10.023
8. Mazur LP, Cechinel MAP, de Souza SMAGU et al (2018) Brown marine macroalgae as natural cation exchangers for toxic metal removal from industrial wastewaters: A review. J Environ Manage 223:215–253. https://doi.org/10.1016/j.jenvman.2018.05.086
9. Ahmed MJ, Hameed BH (2019) Insights into the isotherm and kinetic models for the coadsorption of pharmaceuticals in the absence and presence of metal ions: A review. J Environ Manage 252:109617. https://doi.org/10.1016/j.jenvman.2019.109617
10. Bazrafshan E, Mohammadi L, Ansari-Moghaddam A, Mahvi AH (2015) Heavy metals removal from aqueous environments by electrocoagulation process - A systematic review. J Environ Heal Sci Eng 13:. https://doi.org/10.1186/s40201-015-0233-8
11. Song P, Yang Z, Zeng G et al (2017) Electrocoagulation treatment of arsenic in wastewaters: A comprehensive review. Chem Eng J 317:707–725. https://doi.org/10.1016/j.cej.2017.02.086
12. Zakir O, Idouhli R, Elyaagoubi M, et al (2020) Fabrication of TiO2Nanotube by Electrochemical Anodization: Toward Photocatalytic Application. J Nanomater 2020:. https://doi.org/10.1155/2020/4745726
13. Reddy EP, Davydov L, Smirniotis P (2003) TiO2-loaded zeolites and mesoporous materials in the sonophotocatalytic decomposition of aqueous organic pollutants: the role of the support. Appl Catal B Environ 42:1–11. https://doi.org/10.1016/S0926-3373(02)00192-3
14. Badvi K, Javanbakht V (2021) Enhanced photocatalytic degradation of dye contaminants with TiO2 immobilized on ZSM-5 zeolite modified with nickel nanoparticles. J Clean Prod 280:124518. https://doi.org/10.1016/j.jclepro.2020.124518
15. Kanakaraju D, Kockler J, Motti CA et al (2015) Titanium dioxide/zeolite integrated photocatalytic adsorbents for the degradation of amoxicillin. Appl Catal B Environ 166–167:45–55. https://doi.org/10.1016/J.APCATB.2014.11.001
16. Ahmad R, Ahmad Z, Khan AU et al (2016) Photocatalytic systems as an advanced environmental remediation: Recent developments, limitations and new avenues for applications. J Environ Chem Eng 4:4143–4164. https://doi.org/10.1016/J.JECE.2016.09.009

17. Vamathevan V, Amal R, Beydoun D et al (2002) Photocatalytic oxidation of organics in water using pure and silver-modified titanium dioxide particles. J Photochem Photobiol A Chem 148:233–245. https://doi.org/10.1016/S1010-6030(02)00049-7
18. Zakir O, Karra AA, Elyaagoubi RIM et al (2022) Fabrication and characterization of Ag - and Cu - doped TiO 2 nanotubes (NTs) by in situ anodization method as an efficient photocatalyst. J Solid State Electrochem. https://doi.org/10.1007/s10008-022-05237-4
19. Nezamzadeh-Ejhieh A, Khorsandi S (2014) Photocatalytic degradation of 4-nitrophenol with ZnO supported nano-clinoptilolite zeolite. J Ind Eng Chem 20:937–946. https://doi.org/10.1016/j.jiec.2013.06.026
20. Nezamzadeh-Ejhieh A, Salimi Z (2011) Solar photocatalytic degradation of o-phenylenediamine by heterogeneous CuO/X zeolite catalyst. Desalination 280:281–287. https://doi.org/10.1016/j.desal.2011.07.021
21. Kuwahara Y, Aoyama J, Miyakubo K et al (2012) TiO2 photocatalyst for degradation of organic compounds in water and air supported on highly hydrophobic FAU zeolite: Structural, sorptive, and photocatalytic studies. J Catal 285:223–234. https://doi.org/10.1016/J.JCAT.2011.09.031
22. Wang CC, Lee CK, Du LM, Juang LC (2008) Photocatalytic degradation of C.I. Basic Violet 10 using TiO2 catalysts supported by Y zeolite: An investigation of the effects of operational parameters. Dye Pigment 76:817–824. https://doi.org/10.1016/J.DYEPIG.2007.02.004
23. Torkian N, Bahrami A, Hosseini-Abari A et al (2022) Synthesis and characterization of Ag-ion-exchanged zeolite/TiO2 nanocomposites for antibacterial applications and photocatalytic degradation of antibiotics. Environ Res 207:112157. https://doi.org/10.1016/J.ENVRES.2021.112157
24. Alakhras F, Alhajri E, Haounati R et al (2020) A comparative study of photocatalytic degradation of Rhodamine B using natural-based zeolite composites. Surfaces and Interfaces 20:100611. https://doi.org/10.1016/j.surfin.2020.100611
25. Li F, Jiang Y, Yu L et al (2005) Surface effect of natural zeolite (clinoptilolite) on the photocatalytic activity of TiO2. Appl Surf Sci 252:1410–1416. https://doi.org/10.1016/J.APSUSC.2005.02.111
26. Khanmohammadi M, Rahmani F, Rahbar Shahrouzi J, Akbari Sene R (2024) Insightful properties-performance study of Ti–Cu–O heterojunction sonochemically embedded in mesoporous silica matrix for efficient tetracycline adsorption and photodegradation: RSM and ANN-based modeling and optimization. Chemosphere 352:141223. https://doi.org/10.1016/J.CHEMOSPHERE.2024.141223
27. Moradi M, Sene RA, Rahmani F, Rezakazemi M (2023) Efficient photodegradation of paraquat herbicide over TiO2-WO3 heterojunction embedded in diatomite matrix and process optimization. Environ Sci Pollut Res 30:99675–99693. https://doi.org/10.1007/S11356-023-29306-X/METRICS
28. Haghighi M, Rahmani F, Kariminejad F, Akbari Sene R (2019) Photodegradation of lignin from pulp and paper mill effluent using TiO2/PS composite under UV-LED radiation: Optimization, toxicity assessment and reusability study. Process Saf Environ Prot 122:48–57. https://doi.org/10.1016/J.PSEP.2018.11.020
29. Mintova S, Valtchev V (2002) Effect of the silica source on the formation of nanosized silicalite-1: an in situ dynamic light scattering study. Microporous Mesoporous Mater 55:171–179. https://doi.org/10.1016/S1387-1811(02)00401-8
30. Moneim MA, Ahmed EA (2015) Synthesis of Faujasite from Egyptian Clays: Characterizations and Removal of Heavy Metals. Geomaterials 05:68–76. https://doi.org/10.4236/GM.2015.52007
31. Wajima T, Yoshizuka K, Hirai T, Ikegami Y Synthesis of Zeolite X from Waste Sandstone Cake Using Alkali Fusion Method. https://doi.org/10.2320/matertrans.MRA2007250
32. Ait baha A, Tabit K, Idouhli R, et al (2023) Effect of Liquor/(Si/Al) Ratio on Zeolite Synthesis from Fumed Silica and Coal Fly Ash Using the Taguchi Approach. Chem Africa. https://doi.org/10.1007/s42250-023-00805-1
33. Huang M, Xu C, Wu Z et al (2008) Photocatalytic discolorization of methyl orange solution by Pt modified TiO2 loaded on natural zeolite. Dye Pigment 77:327–334. https://doi.org/10.1016/j.dyepig.2007.01.026
34. Salazar H, Nunes-Pereira J, Correia DM et al (2016) Poly(vinylidene fluoride-hexafluoropropylene)/bayerite composite membranes for efficient arsenic removal from water. Mater Chem Phys 183:430–438. https://doi.org/10.1016/J.MATCHEMPHYS.2016.08.049
35. Jia Y, Zhu BS, Jin Z et al (2015) Fluoride removal mechanism of bayerite/boehmite nanocomposites: Roles of the surface hydroxyl groups and the nitrate anions. J Colloid Interface Sci 440:60–67. https://doi.org/10.1016/J.JCIS.2014.10.069
36. Violante A, Ricciardella M, Pigna M, Capasso R (2005) Effects of Organic Ligands on the Adsorption of Trace Elements onto Metal Oxides and Organo-Mineral Complexes. Biogeochem Trace Elem Rhizosph 157–182. https://doi.org/10.1016/B978-044451997-9/50007-6
37. Nunes-Pereira J, Lima R, Choudhary G et al (2018) Highly efficient removal of fluoride from aqueous media through polymer composite membranes. Sep Purif Technol 205:1–10. https://doi.org/10.1016/J.SEPPUR.2018.05.015
38. Yang Z, Cai W (2020) Surfactant-free preparation of mesoporous solid/hollow boehmite and bayerite microspheres via double hydrolysis of NaAlO2 and formamide from room temperature to 180 °C. J Colloid Interface Sci 564:182–192. https://doi.org/10.1016/J.JCIS.2019.12.110
39. Rida K, Bouraoui S, Hadnine S (2013) Adsorption of methylene blue from aqueous solution by kaolin and zeolite. Appl Clay Sci 83–84:99–105. https://doi.org/10.1016/J.CLAY.2013.08.015
40. Qiang Z, Shen X, Guo M et al (2019) A simple hydrothermal synthesis of zeolite X from bauxite tailings for highly efficient adsorbing CO2 at room temperature. Microporous Mesoporous Mater 287:77–84. https://doi.org/10.1016/J.MICROMESO.2019.05.062
41. Rao KVS, Subrahmanyam M, Boule P (2004) Immobilized TiO2 photocatalyst during long-term use: decrease of its activity. Appl Catal B Environ 49:239–249. https://doi.org/10.1016/J.APCATB.2003.12.017
42. Zhong L, Haghighat F (2015) Photocatalytic air cleaners and materials technologies – Abilities and limitations. Build Environ 91:191–203. https://doi.org/10.1016/J.BUILDENV.2015.01.033
43. Portela R, Jansson I, Suárez S et al (2017) Natural silicate-TiO2 hybrids for photocatalytic oxidation of formaldehyde in gas phase. Chem Eng J 310:560–570. https://doi.org/10.1016/J.CEJ.2016.06.018
44. Zulmajdi SLN, Ajak SNFH, Hobley J, et al (2017) 1–6 of Photocatalytic Degradation of Methylene Blue in Aqueous Dispersions of TiO 2 Nanoparticles under UV-LED Irradiation. Am J Nanomater 5:1–6. https://doi.org/10.12691/ajn-5-1-1
45. Gomes da Silva C, Faria JL (2003) Photochemical and photocatalytic degradation of an azo dye in aqueous solution by UV irradiation. J Photochem Photobiol A Chem 155:133–143. https://doi.org/10.1016/S1010-6030(02)00374-X
46. Nibou D, Mekatel H, Amokrane S et al (2010) Adsorption of Zn2+ ions onto NaA and NaX zeolites: Kinetic, equilibrium and thermodynamic studies. J Hazard Mater 173:637–646. https://doi.org/10.1016/J.JHAZMAT.2009.08.132
47. Introduction to Zeolite Molecular Sieves - Jiri Cejka, Herman van Bekkum, A. Corma, F. Schueth - Google Livres. https://books.google.co.ma/books?hl=fr&lr=&id=x750AvzG_egC&oi=fnd&pg=PP1&dq=Zeolite+molecular+sieves:+structure,+chemistry,+and+use&ots=KfkibiUUU5&sig=8DG7lk_Ypsmrbc7DpxKrHN

i49ZA&redir_esc=y#v=onepage&q=Zeolite molecular sieves%3A structure%2C chemistry%2C and use&f=false. Accessed 27 Sep 2022
48. Rahmani F, Haghighi M (2016) One-pot hydrothermal synthesis of ZSM-5-CeO2 composite as a support for Cr-based nanocatalysts: Influence of ceria loading and process conditions on CO2-enhanced dehydrogenation of ethane. RSC Adv 6:89551–89563. https://doi.org/10.1039/C6RA15787D
49. Rahmani F, Haghighi M (2016) C2H6/CO2 oxidative dehydrogenation (ODH) reaction on nanostructured CrAPSO-34 catalyst: One-pot hydrothermal vs. conventional hydrothermal/impregnation catalyst synthesis. Korean J Chem Eng 33:2555–2566. https://doi.org/10.1007/S11814-016-0125-3
50. Huang Y, Wang K, Dong D et al (2010) Synthesis of hierarchical porous zeolite NaY particles with controllable particle sizes. Microporous Mesoporous Mater 127:167–175. https://doi.org/10.1016/J.MICROMESO.2009.07.026
51. Ait Baha A, Tabit K, Idouhli R et al (2023) Zeolitization of Fumed Silica and Coal Fly Ash Using the Taguchi Method Toward Organic Pollutant Removal. SILICON 2023:1–12. https://doi.org/10.1007/S12633-023-02501-8
52. Delir Kheyrollahi Nezhad P, Haghighi M, Jodeiri N, Rahmani F (2016) Sol–gel preparation of NiO/ZrO2(x)–MgO(100–x) nanocatalyst used in CO2/O2 oxidative dehydrogenation of ethane to ethylene: influence of Mg/Zr ratio on catalytic performance. J Sol-Gel Sci Technol 80:436–450. https://doi.org/10.1007/S10971-016-4120-2
53. Rocha J, Klinowski J, Adams JM (1991) Synthesis of zeolite Na-A from metakaolinite revisited. J Chem Soc Faraday Trans 87:3091–3097. https://doi.org/10.1039/FT9918703091
54. Molina A, Poole C (2004) A comparative study using two methods to produce zeolites from fly ash. Miner Eng 17:167–173. https://doi.org/10.1016/J.MINENG.2003.10.025
55. Kikuchi S, Saeki T, Ishida M et al (1979) The Chemistry of Silica. Solubility, Polym Colloid Surf Prop Biochem Silica 38:209–214. https://doi.org/10.1678/RHEOLOGY.38.209
56. Gimeno D (2011) Synthesis and characterization of Na-X, Na-A and Na-P zeolites and hydroxysodalite from metakaolinite. Clay Miner 46:339–354. https://doi.org/10.1180/claymin.2011.046.3.339
57. Zhang G, Song A, Duan Y, Zheng S (2018) Enhanced photocatalytic activity of TiO2/zeolite composite for abatement of pollutants. Microporous Mesoporous Mater 255:61–68. https://doi.org/10.1016/j.micromeso.2017.07.028
58. Zakir O, Mouchtari E, Elyaagoubi M, Rachid L (2022) Anodic TiO 2 nanotube : influence of annealing temperature on the photocatalytic degradation of carbamazepine. https://doi.org/10.1007/s41779-022-00752-z
59. Kurata T, Sakurai Y (1967) Degradation of L-Ascorbic Acid and Mechanism of Nonenzymic Browning Reaction. Agric Biol Chem 31:170–184. https://doi.org/10.1080/00021369.1967.10858792
60. Setthaya N, Chindaprasirt P, Yin S, Pimraksa K (2017) TiO2-zeolite photocatalysts made of metakaolin and rice husk ash for removal of methylene blue dye. Powder Technol 313:417–426. https://doi.org/10.1016/J.POWTEC.2017.01.014
61. Mahamud M, Taddesse AM, Bogale Y, Bezu Z (2023) Zeolite supported CdS/TiO2/CeO2 composite: Synthesis, characterization and photocatalytic activity for methylene blue dye degradation. Mater Res Bull 161:112176. https://doi.org/10.1016/J.MATERRESBULL.2023.112176
62. Wardhani S, Rahman MF, Purwonugroho D, et al (2016) Photocatalytic Degradation of Methylene Blue Using TiO 2-Natural Zeolite as A Photocatalyst. J Pure App Chem Res 5:19–27. https://doi.org/10.21776/ub.jpacr.2016.005.01.232
63. Nagarjuna R, Challagulla S, Alla N et al (2015) Synthesis and characterization of reduced-graphene oxide/TiO2/Zeolite-4A: A bifunctional nanocomposite for abatement of methylene blue. Mater Des 86:621–626. https://doi.org/10.1016/J.MATDES.2015.07.116
64. Tayade RJ, Kulkarni RG, Jasra RV (2007) Enhanced photocatalytic activity of TiO2-Coated NaY and HY zeolites for the degradation of methylene blue in water. Ind Eng Chem Res 46:369–376. https://doi.org/10.1021/IE060641O
65. Taghvaei H, Farhadian M, Davari N, Maazi S (2017) Preparation, characterization and photocatalytic degradation of methylene blue by Fe3+ doped TiO2 supported on natural zeolite using response surface methodology. Adv Environ Technol 3:205–216. https://doi.org/10.22104/AET.2018.2462.1124
66. Baouali NY, Nibou D, Amokrane S (2022) NaY Zeolite and TiO2 Impregnated NaY Zeolite for the Adsorption and Photocatalytic Degradation of Methylene Blue under Sunlight. Iran J Chem Chem Eng 41:1907–1920. https://doi.org/10.30492/IJCCE.2021.128624.4168